Electronic Supplementary Information

Controlled Synthesis and Raman Study of 2D Antiferromagnetic P-type Semiconductor: α-MnSe

Ningning Li,‡[a,d] Leilei Zhu,‡[b] Honghui Shang,‡[b] Feng Wang,[a] Yu Zhang,[a] Yuyu Yao,[a,d] Junjun Wang,[a] Xueying Zhan,[a] Fengmei Wang,[a] Jun He,[a,c,d] and Zhenxing Wang,*[a,d]

[a]CAS Center for Excellence in Nanoscience, CAS Key Laboratory of Nanosystem and Hierarchical Fabrication, National Center for Nanoscience and Technology, Beijing 100190, P. R. China

[b]The Institute of Computing Technology, Chinese Academy of Sciences, Beijing 100049, P. R. China

[c]Key Laboratory of Artificial Micro- and Nano-structures of Ministry of Education, School of Physics and Technology, Wuhan University, Wuhan 430072, P. R. China.

[d]Sino-Danish College, Sino-Danish Center for Education and Research, University of Chinese Academy of Sciences, Beijing 100049, P. R. China

†Electronic supplementary information (ESI) available. See DOI:

‡These authors contributed equally to this work.

*Correspondence and requests for materials should be addressed to Z. W. (email: wangzx@nanoctr.cn).

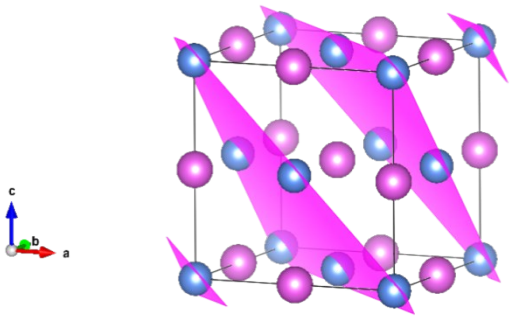

Fig. S1. The magnetic orderings of a Mn sublattice is used to show the magnetic structures of α-MnSe. Blue sites are Mn atoms and red sites are Se atoms.

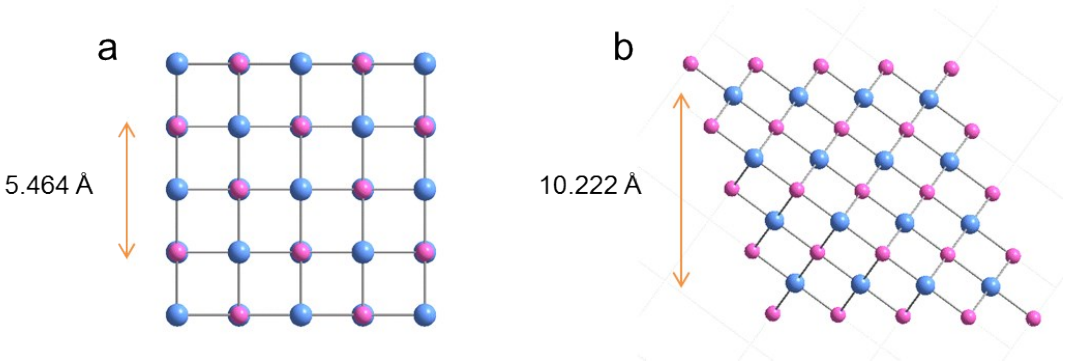

Fig. S2. (a) The side view of α-MnSe (001), the thickness of the unit cell is 5.464Å. (b) The side view of α-MnSe (111), the thickness of the unit cell 10.222 Å.

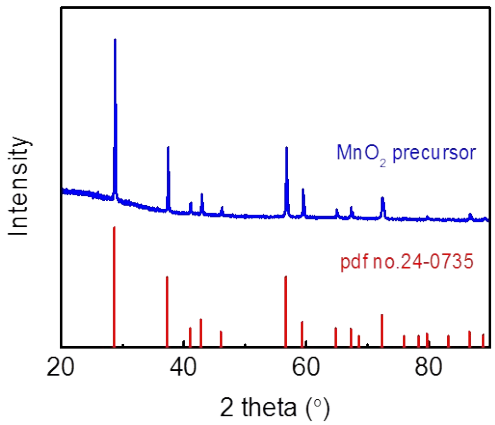

Fig. S3. XRD pattern for MnO_2 powder as Mn source.

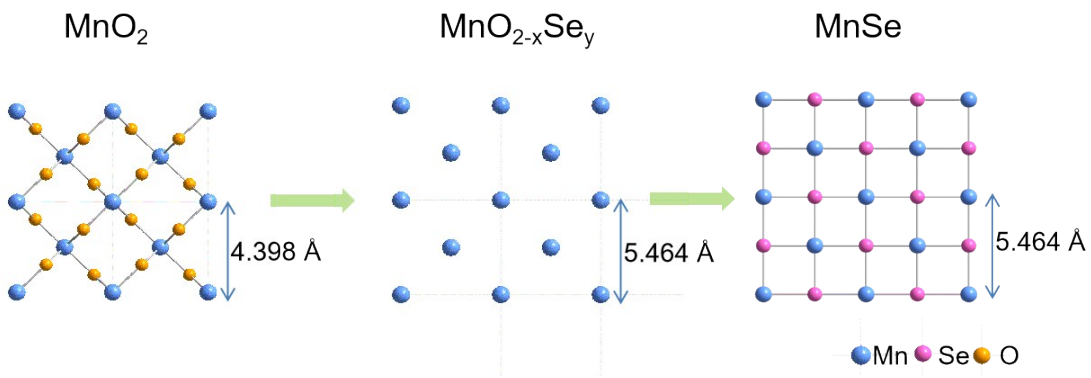

Fig. S4. Schematic represents the formation of MnSe from MnO_2 in a CVD process.

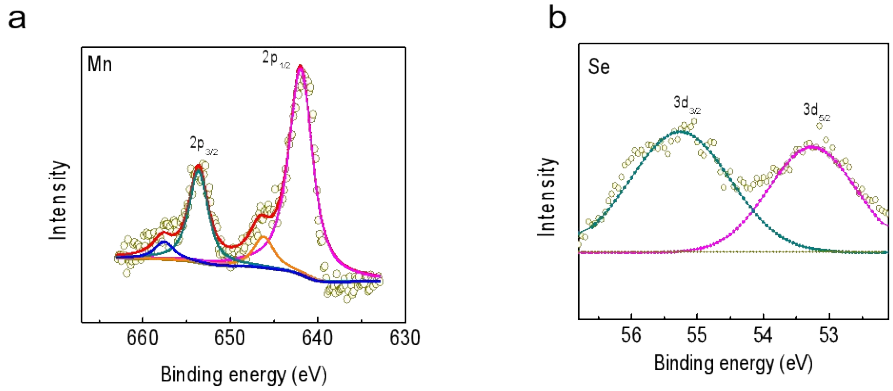

Fig. S5. XPS characterization of Mn 2p and Se 3d of as-grown square α-MnSe.

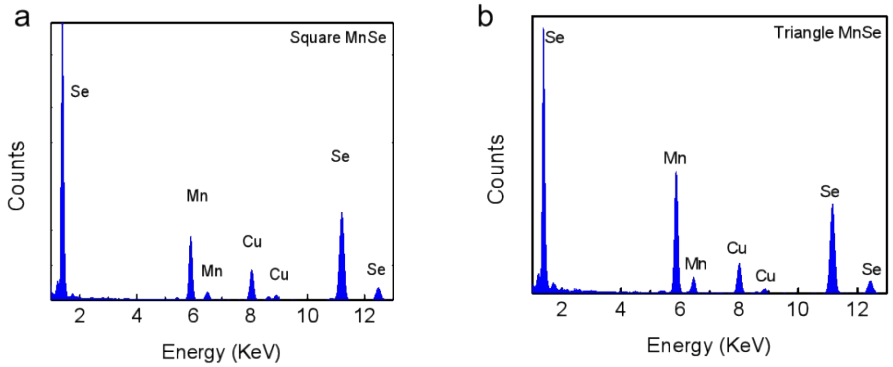

Fig. S6. (a, b) Elemental analysis of the square and triangular α-MnSe nanosheets on copper grids, respectively.

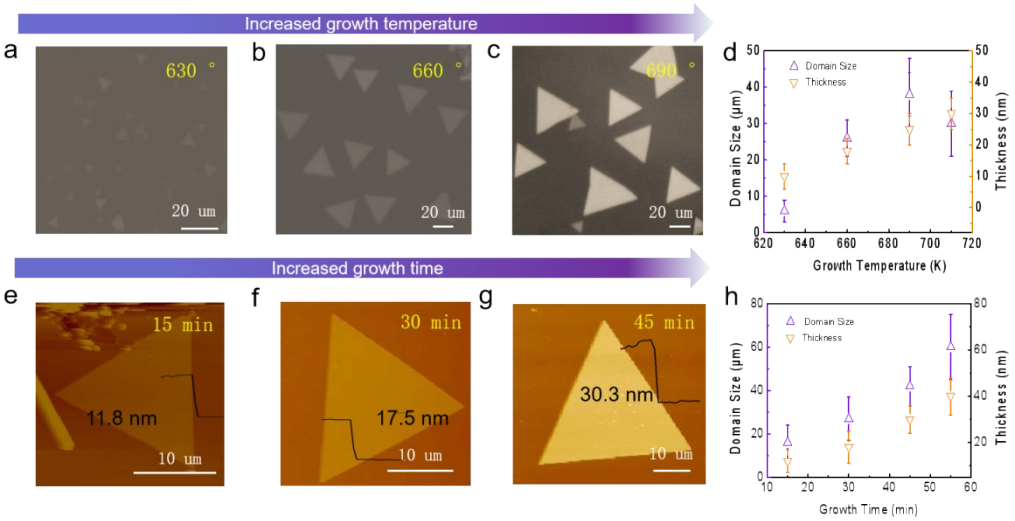

Fig. S7. Modulation of triangular α-MnSe nanosheets in size and thickness. (a–c) OM images of α-MnSe triangular nanosheets grown for 30 min at 630°C, 660 °C, and 690 °C, respectively. Scale bar: 20 μm. (d) Temperature-dependent on domain size and thickness of as-grown triangular α-MnSe nanosheets. (e–g) AFM images of triangular α-MnSe nanosheets grown at different growth times of 15, 30, and 45 min under growth temperature of 660 °C. Scale bar: 10 μm. (h) Growth time-dependent on domain size and thickness of as-grown triangular α-MnSe nanosheets.

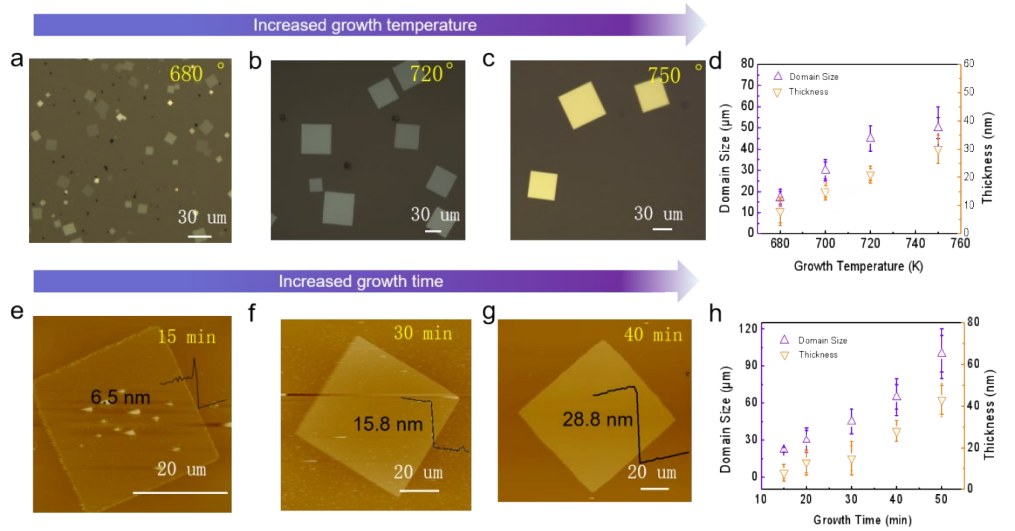

Fig. S8. Modulation of square α-MnSe nanosheets in size and thickness. (a–c) OM images of square α-MnSe nanosheets grown for 30 min at 680°C, 720 °C, and 750 °C, respectively. Scale bar: 30 μm. (d) Temperature-dependent on domain size and thickness of as-grown square α-MnSe nanosheets. (e–g) AFM images of square α-MnSe nanosheets grown at different growth times of 15, 30, and 45 min under growth temperature of 720 °C. Scale bar: 20 μm. (h) Growth time-dependent on domain size and thickness of as-grown square α-MnSe nanosheets.

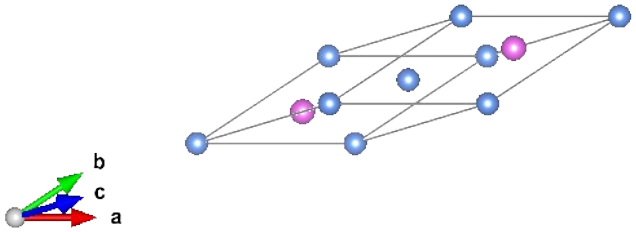

Fig. S9. The AFM primitive cell consisting of 2 Mn atoms (blue spheres) and 2 Se atoms (red spheres).

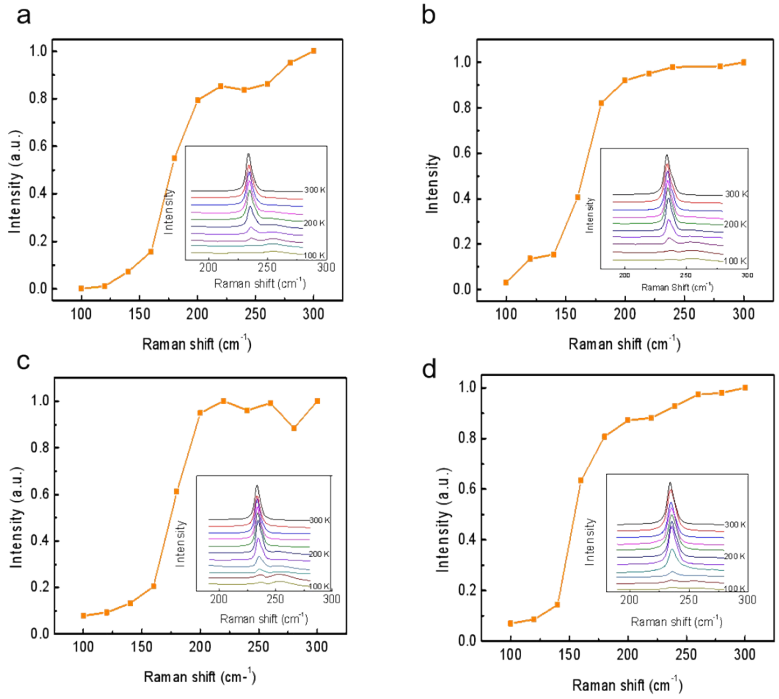

Fig. S10. (a, b) Raman intensity changes with temperatures in triangular α-MnSe nanosheets at thickness of 15.5 nm and 30.5 nm, respectively. (c, d) Raman intensity changes with temperatures in square α-MnSe nanosheets at thickness of 17.8 nm and 34.5 nm, respectively.

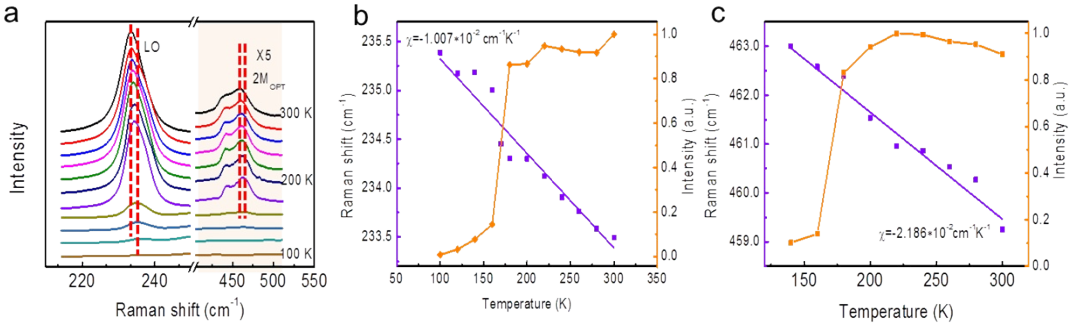

Fig. S11. (a) Temperature-dependent Raman spectra of square α-MnSe nanosheets. (b, c) Detailed plots of Raman position and intensity variation to temperature of LO and $2M_{OPT}$

modes, respectively. The dots are the experimental data and the linear lines refer to the fitting data. The extracted temperature coefficients χ are shown.

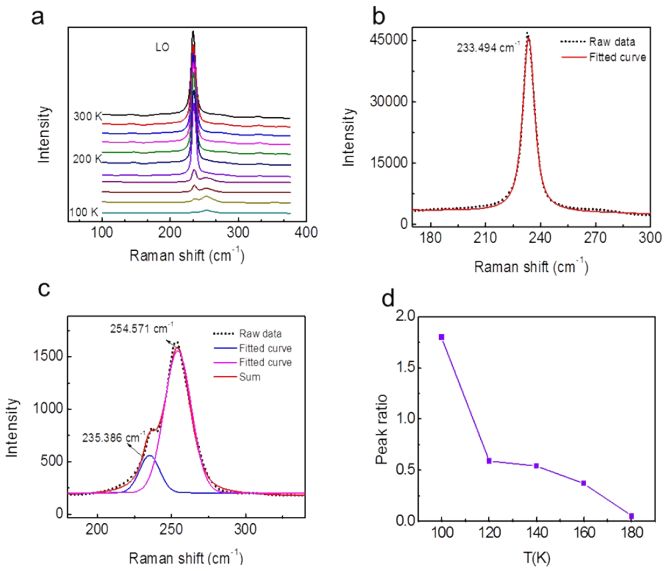

Fig. S12. (a) Raman peaks of square α-MnSe nanosheets from 100 K to 300 K. (b) LO mode at 300 K. (c) LO mode and Raman peak at 254 cm^{-1} at 100K. (d) Plots of peak intensity ratio of 254 cm^{-1} /234 cm^{-1} versus temperatures.

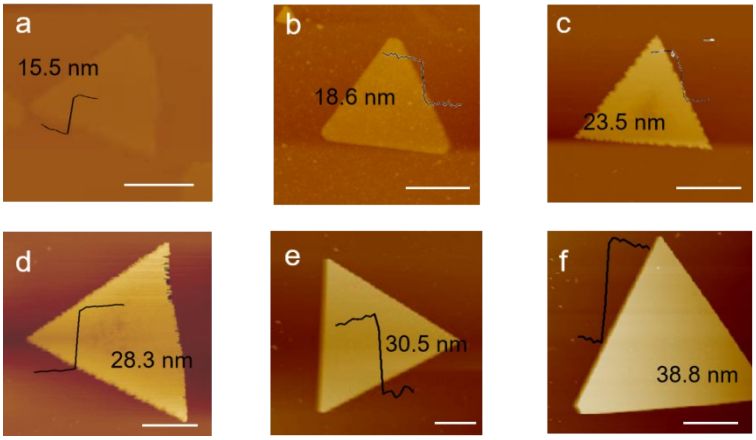

Fig. S13. AFM images of triangular α-MnSe nanosheets for thickness-dependent Raman measurement. Scale bar : 2 μm.

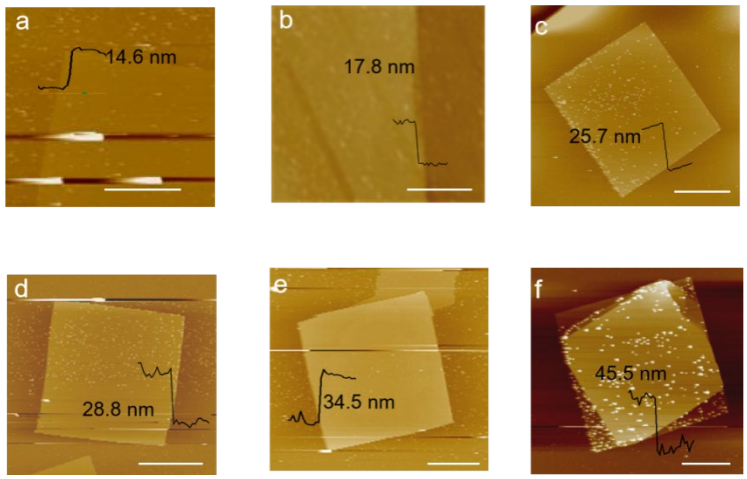

Fig. S14. AFM images of square α-MnSe nanosheets for thickness-dependent Raman measurement. Scale bar :2 μm.

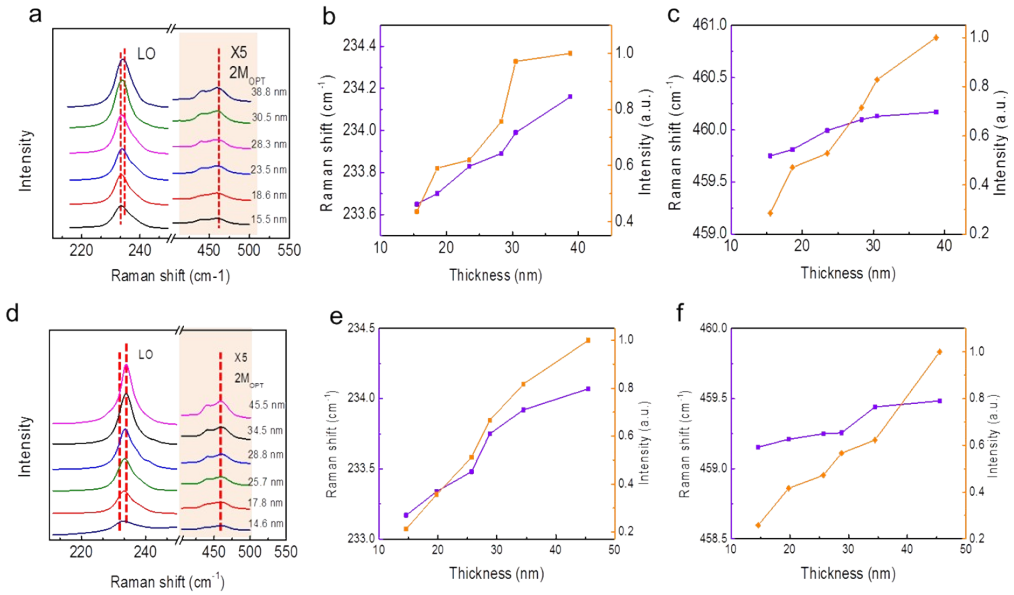

Fig. S15. Thickness-dependent Raman spectra of triangular a) and square d) nanosheets. Detailed plots of Raman position and intensity variation to thickness of LO and $2M_{OPT}$ modes of triangular b,c) and square e,f), respectively. The purple points and curves represent Raman shift, the orange points and curves correspond to normalized Raman intensity.

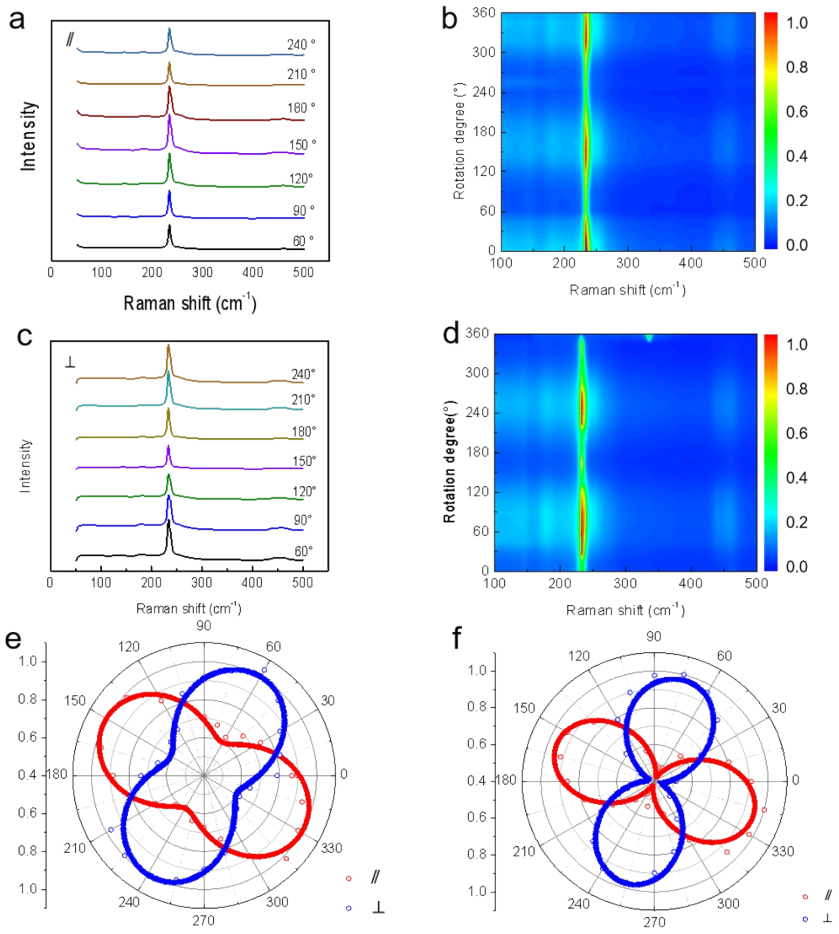

Fig. S16. Angle-resolved polarized Raman spectra of square α-MnSe nanosheets. (a, c) Polarization-dependent Raman intensity of square α-MnSe nanosheets in the parallel and cross polarization configurations, respectively. (b, d) False-color image of the polarized Raman spectra of square α-MnSe nanosheets in the parallel and cross polarization configurations, respectively. The color scale stands for Raman intensity. (e, f) Polar figures of the fitted peak intensity of LO and $2M_{OPT}$ Raman modes as a function of rotation degree in the parallel and cross polarization configurations. The scattered circles are the experimental data and the solid lines are the fitting results. The intensity of each mode is normalized to its maximum value.

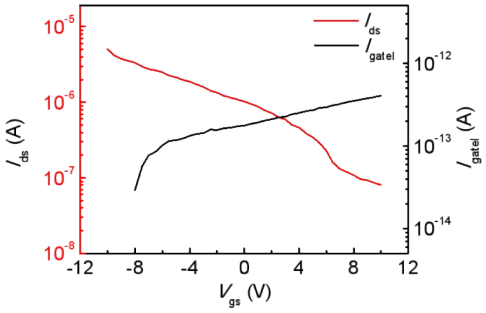

Fig. S17. Transfer curve of a typical α-MnSe transistor.

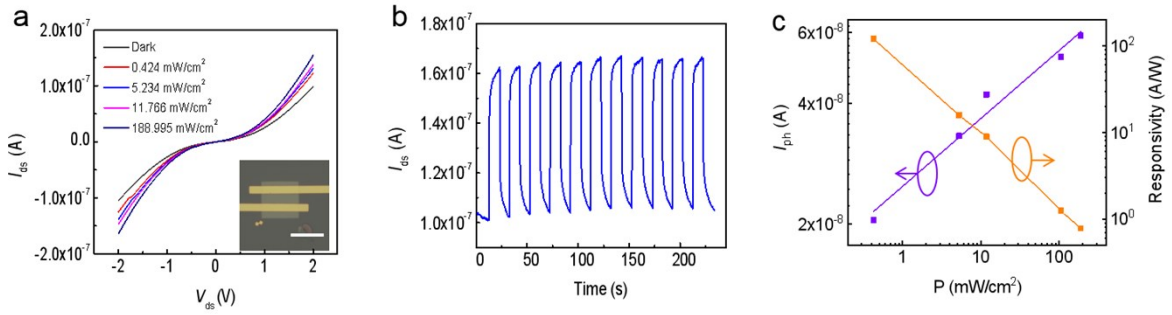

Fig. S18. Optoelectronic properties of square α-MnSe photodetetcors. (a) Output characteristic curves of α-MnSe photodetector in dark and under different illuminated power densities. The inset is the AFM image of the measured device. (b) Photoswitching behavior of α-MnSe photodetetcor under periodic illumination at power density of 188.995 mW/cm^2. (c) Photocurrent (I_{ph}) and Responsivity (R) as a function of incident power densities (P) at V_{ds} = 1 V. The linear line is the corresponding fitting curve.

Table S1. The influence of different U values on the band gap in GGA method. Lattice constant a corresponds to the primitive cell in Figure S9.

U (eV)	0	1	2	3	4	6	8	10
Lattice a (Å)	6.583	6.632	6.672	6.706	6.736	6.785	6.822	6.849
Band Gap (eV)	0.5717	1.0098	1.3531	1.4777	1.5278	1.5847	1.6244	1.662

Table S2. The calculated phonon frequency with different U values in GGA (U=0) and GGA+U method.

Frequency	U (eV)							
	0	1	2	3	4	6	8	10
1	0	0	0	0	0	0	0	0
2	0	0	0	0	0	0	0	0
3	0	0	0	0	0	0	0	0
4	88	89	90	90	90	91	92	92
5	88	89	90	90	90	91	92	92
6	98	107	112	115	117	119	121	122
7	98	107	112	115	117	119	121	122
8 (TO)	102	117	124	128	130	133	135	136
9 (TO)	102	117	124	128	130	133	135	136
10	169	169	169	169	168	167	166	166
11	171	183	190	195	199	203	205	207
12 (LO)	202	210	215	218	220	222	223	223

Table S3. The influence of GGA-PBE and LDA functionals on the calculation accuracy.

Frequency	PBE (U = 0)	LDA (U = 0)	PBE + U (2 eV)	LDA + U (2 eV)	PBE + U (8 eV)	LDA + U (8 eV)
1	0	0	0	0	0	0
2	0	0	0	0	0	0
3	0	0	0	0	0	0
4	88	98	90	106	92	106
5	88	98	90	106	92	106
6	98	98	112	118	121	134
7	98	98	112	118	121	134
8	102	105	124	139	135	157
9	102	105	124	139	135	157
10	169	148	169	181	166	177
11	171	181	190	189	205	215
12	202	205	215	224	223	236